Orbit Determination of Resident Space Objects with the Multibeam Radar Sensor BIRALES

Matteo Losacco, Pierluigi Di Lizia, Mauro Massari*
Politecnico di Milano, Milano, 20156, Italy

Andrea Mattana, Federico Perini, Marco Schiaffino, Claudio Bortolotti, Mauro Roma, Giovanni Naldi, Giuseppe Pupillo, Germano Bianchi†
Istituto Nazionale di Astrofisica, Bologna, 40129, Italy.

Denis Cutajar, Alessio Magro‡
University of Malta, Msida, MSD 2080, Malta.

Claudio Portelli§
Italian Space Agency, Roma, 00133, Italy

Marco Reali, Walter Villadei¶
Italian Air Staff-ITAF, Roma, 00185, Italy.

Near-Earth space has become progressively more crowded in active satellites, inactive spacecraft and debris. Consequently, an international effort is currently being devoted to improving the performance of the network of optical and radar sensors for space objects monitoring. Within this framework, the use of the novel bistatic radar sensor BIRALES is investigated in this work, which makes use of a multibeam receiver. The tailored orbit determination algorithm is described, which receives as input the data processed by the acquisition system, that digitally assembles measured radar echoes. The performance of the orbit determination process is assessed on a set of numerical simulations carried out on the NORAD catalogue, using a dedicated simulator of the sensor and considering both cases of known and unknown objects, with single or repeated passages on the receiver sensor.

I. Introduction

The number of manmade objects orbiting the Earth has dramatically increased during the last decades, posing a serious risk for space based activities (Ref. [1]). Most of the objects currently orbiting the Earth are classified as space debris and include inactive satellites, discarded launch stages, and fragments originated from satellite breakups and collisions. Several counter measures have been adopted with the aim of reducing mission related risks and casualties and to control the number of objects in orbit. Mitigation guidelines have been published by various organisations such as the Inter-Agency Space Debris Coordination (IADC) committee and the United Nations (UN). In parallel specific space programs were started to build the expertise required to manage the challenges posed by the space traffic control problem. Collision risk assessment is performed daily by satellite operators and conjunction summary messages are provided to satellite operators by the United States Strategic Command (USSTRATCOM) to support decisions on the execution of collision avoidance manoeuvres (Ref. [2]). In addition, re-entry predictions of objects are regularly produced to estimate on ground risks (Ref. [3]). Both collision risk assessment and re-entry predictions rely on the accurate estimation of the state of the orbiting objects and of their evolution, which is derived from the tracking of the space objects using dedicated optical, radar, and laser sensors.

*{Ph.D. Candidate, Assistant Professor, Assistant Professor}, Department of Aerospace Science and Technology, Via G. La Masa 34, Milano, Italy, {matteo.losacco, pierluigi.dilizia, mauro.massari}@polimi.it

†{Technician, Research Engineer, Technician, Technician, Technician, Research Engineer, Research Astronomer, Research Engineer}, Istituto di Radioastronomia, Via P. Gobetti 101, Bologna, Italy, {mattana, f.perini, m.schiaffino, c.bortolotti, m.roma, gnaldi, g.pupillo, gbianchi}@ira.inaf.it

‡{Research Support Officer, Lecturer}, Institute of Space Sciences and Astronomy, Msida MSD 2080, Malta, {denis.cutajar, alessio.magro}@um.edu.mt

§Technical Manager, via del Politecnico snc, Roma, Italy, claudio.portelli@asi.it

¶{Maj., Lt.Col.}, Italian Air Force Space Policy Office, Viale dell'Università 4, Roma, Italy, {marco.reali, walter.villadei}@aeronautica.difesa.it

Survey and tracking of objects in Earth orbit is one of the main areas where the European Space Surveillance and Tracking (SST) Support Framework and the ESA Space Situational Awareness (SSA) programmes are active (Ref. [4, 5]), with the aim of implementing a European network of sensors for surveillance and tracking of objects in Earth's orbit. Within this framework, the Italian Northern Cross radio telescope array has been upgraded to serve the European SST Framework as a component of the Italian contribution to the European network for SST in the frame of the BIstatic RAdar for LEo Survey (BIRALES) sensor (Ref. [6]).

BIRALES uses part of the Northern Cross radiotelescope located in Medicina (Bologna, Italy) as the receiver. Part of the radiotelescope has been refurbished and a digital backend has been implemented to allow beamforming of 32 beams distributed across the receiver field of view (FoV). When an object transits inside the antenna FoV, the beams are illuminated by the reflected radio wave. Consequently, besides the classical range and Doppler shift measurements, the beam illumination sequence provides an estimate of the transit direction of the scattering object and of the associated angular deviations profiles. The data received from BIRALES are provided as input to a tailored orbit determination (OD) algorithm, which is aimed at computing an estimate of the orbital parameters of the observed object.

A numerical simulator of BIRALES has been developed to assess its performance. Given a catalogue of space objects, the simulator identifies the passages of all the objects in the sensor FoV during a simulated observation campaign. Then, the simulated measurements are generated for each passage and are provided as input to the OD module, along with the required transmitter and receiver information. The simulator is designed so that different kind of transmitter and beams geometry can be easily defined by the user. This enables an effective analysis of the sensitivity of the sensor to its configuration.

This paper illustrates the results achieved with the numerical simulations campaign. The performance of the sensor is assessed using different multibeam configurations and OD algorithms. For each configuration, the simulation is run on a catalogue of Two Line Elements (TLEs) downloaded from Space-Track (`www.space-track.org`). In addition, both the case of known objects (first guess for the OD process generated from the TLE) and unknown objects (first guess for the OD process generated from the measurements) are investigated, and the performance of the sensor is assessed on single and multiple passages of the same object.

II. Bistatic Radar for LEO Survey (BIRALES) Sensor

Ground-based radars provide a powerful tool for the characterization of the orbital debris environment. Radars can in fact irradiate at any time a satellite or space debris in Earth orbit with a microwave beam. The scattered wave can be detected by a receiver, which may be the same transmitting antenna (monostatic radar) or a different one located at a distance of up to several hundreds of kilometers away (bistatic radar).

BIRALES sensor is a bistatic radar composed of two distinct antennas, a receiving and a transmitting one with a baseline of about 580 km. A detailed explanation of the system architecture is provided hereafter and follows the description presented in [7, 8].

The transmitting antenna of BIRALES sensor is the Radio Frequency Transmitter (TRF, see Fig. 1), which is located at the Italian Joint Test Range of Salto di Quirra (PISQ) in Sardinia. It consists of a powerful amplifier able to supply a maximum power of 10 kW in the bandwidth 410-415 MHz. It is a 7 m dish completely steerable at a maximum speed of 3 deg/s and with right hand circular polarization. It is available for operation 24 h/day. Its field of view matches almost perfectly the receiving antenna one, with a beam of 6 deg.

The receiving antenna is a portion of the Northern Cross Radio Telescope (Fig. 2), which is currently one of the largest UHF-capable antenna in the world, being located at the Medicina Radio Astronomical Station, near Bologna, in Northern Italy. It is owned by the University of Bologna but managed and operated by the Istituto di Radioastronomia at the Istituto Nazionale di Astrofisica (INAF-IRA). It consists of two perpendicular branches: the East-West (E/W) arm is 564 m long and consists of a single cylindrical antenna with a width of 35 m, whereas the North-South (N/S) branch is made of 64 parallel antennas with a length of 23.5 m and width of 7.5 m each.

The portion dedicated to BIRALES receiving antenna is actually composed of 16 parabolic cylindrical antennas of the N/S branch (see Fig. 3). The total collecting area is about 2800 m^2 and it allows to detect small objects with sub-metric Radar Cross Section (RCS) at 1000 km of altitude.

BIRALES works in survey mode and exploits an innovative concept based on multibeam technique. Due to the large numbers of receivers installed on the Northern Cross (4 receivers in each N/S antenna for a total of 64 receivers), the FoV can be populated with many independent beams. When an object transits inside the antenna FoV, beams are illuminated by the reflected radio waves. Thus, by looking at the beam illumination sequence, it is possible to estimate the ground track of the transiting objects, with a higher level of details with respect to a single-beam system. The

Fig. 1 Radio frequency transmitter.

Fig. 2 View of the Medicina Radio Astronomical Station. In the foreground, the Northern Cross array.

information about the sequence of illuminated beams allows to discern the trajectory of the object with an estimated orbit accuracy below 100 m.

The system architecture is shown in Fig. 4. Using the TRF it is possible to transmit a power CW signal able to illuminate the target in LEO. The echo radio reflected by the orbital object is received through the Northern Cross and the acquired analog signal is sent to the pre-processing room by an optical fiber link. The digitized data are processed by means of a data acquisition system based on FPGA boards and CPUs, which digitally assembles measured radar echoes using an FFT in spatial domain in order to evaluate the signal detected in each beam. Therefore, Doppler shift, illumination time, antenna pointing angles and measured power intensity associated to each beam are available as well and they are sent to the Italian SST Operation Centre (ISOC) to estimate the orbit of the object detected in a classified environment.

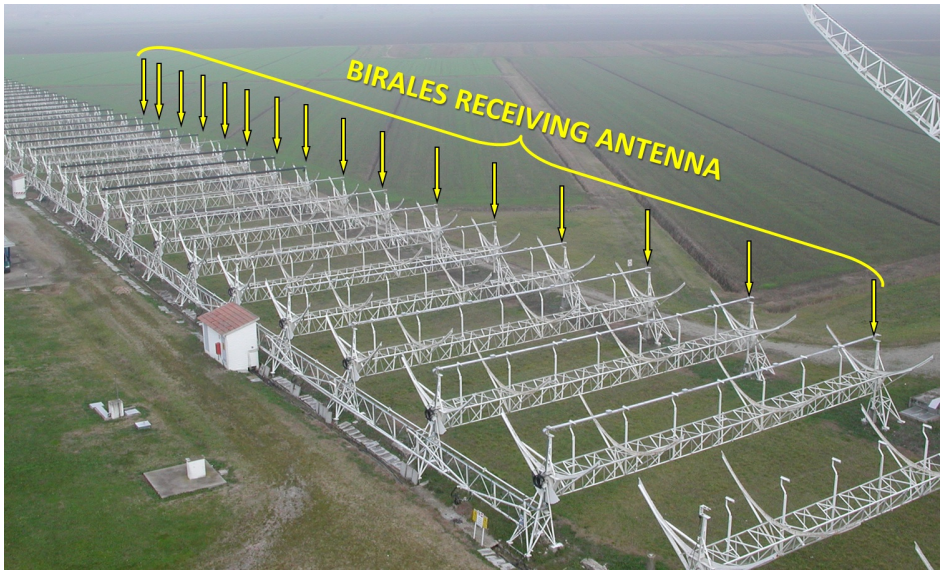

Fig. 3 BIRALES receiving antenna

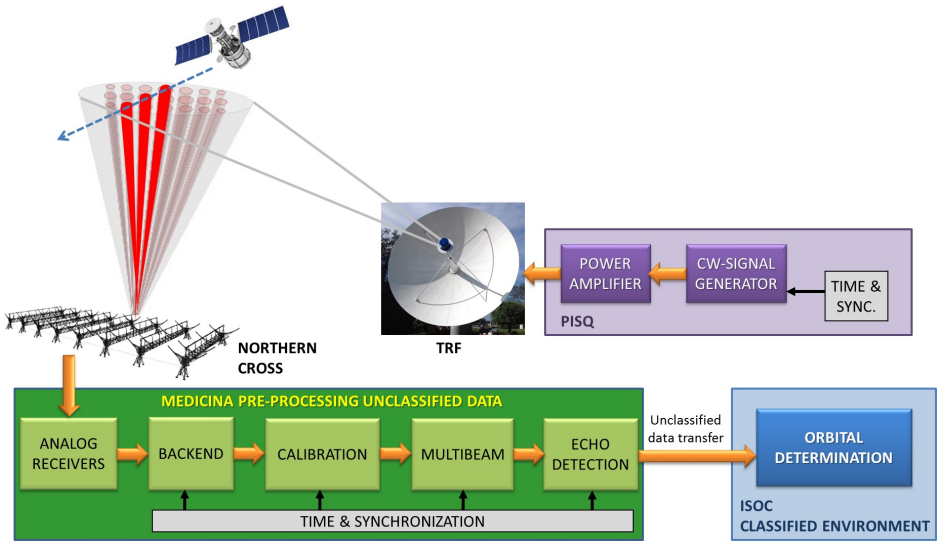

Fig. 4 BIRALES system architecture

A. Analog Receiver

The radio echo received by the Northern Cross is amplified by a front-end board installed on the antenna focal line. The box contains also one electro-optical converter which transmits the analog signal to the pre-processing room by means of the optic fiber link (Fig.5). The front-end performances are:

- NF = 0.45 dB, Tn = 32 K
- Gain = 60 dB
- BW = 16 MHz @408 MHz
- OIP3 > +33 dBm
- InputRL > 15 dB
- OutputRL > 15 dB
- PowerSupply = (10-15) Volt @245 mA

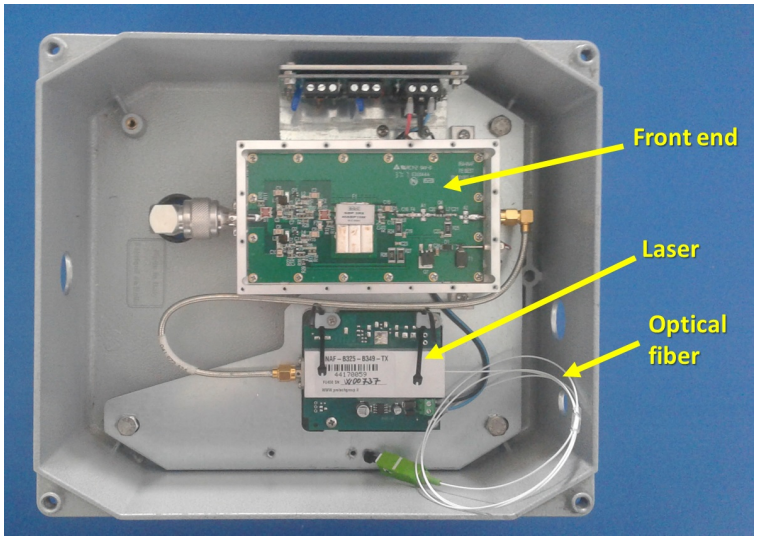

Fig. 5 Box installed on the N/S focal line

B. Backend

The backend system acquires 64 analog signals coming from 64 antenna receivers that need to be digitized by 64 Analog to Digital converters (ADCs). The analog band at the ADCs inputs is 16 MHz centred at 30 MHz (down converted frequency). The data sampled are sent to a first FFT block in order to generate channels with a sample resolution of 78 KHz, that is the maximum space debris Doppler shift. The BIRALES system requires a real-time processing backend which can perform fine channelization of the incoming antenna voltages, pixelate the FoV with multiple coherent beams and process each of these beams for detection of debris echoes. Accurate beam pointing requires the calibration of the array of antennas. Additionally, the system shall be capable of storing and visualizing the results, as well as transmitting them to the orbit determination system. In order to accommodate all these processing stages whilst enabling the addition of new stages with ease, a framework for generating processing pipelines was developed for BIRALES. The pipelining framework makes up the real-time software back-end. This framework allows for the chaining of different software modules into pipelines, the main ones being:

1) The real-time processing pipeline, which receives data from the digital back-end, performs beamforming and channelisation and either writes the resulting data to file or forwards it to the online detection modules for debris detection.
2) The calibration pipeline, which receives data from the digital back-end and correlates the antenna signals together to generate correlation matrices. These are then used by the calibration routine to generate calibration coefficients to compensate for instrumental phase and gain errors.

C. Multibeam

The multibeam pipeline performs fine channelization and multibeaming, such that multiple beams within the array's primary field of view are generated. The resultant beams are then processed by the detection module, which searches for space debris echoes. This pipeline is composed of three software modules: receiver, channelizer, beamformer.

Receiver. The digital backend transmits data to the software backend over a 10 Gb link, containing a single ~78k Hz coarse channel from the 64 antennas. They are transmitted in 32+32 complex fixed point format, which need to be translated to floating point format. The AAVS DAQ library was extended to accept the BIRALES data format and encapsulated as a module. This will read incoming data in chunks and forward the data to the next processing module.

Channelizer. The channel bandwidth is too wide for debris detection, so finer channelization is required. This module implements a polyphase filter bank channelizer, splitting the channel into 8192 ~9.5 Hz separate channels, allowing for a temporal resolution of ~10 samples per second. The number of taps is configurable (more taps require more processing), and each antenna is processed by several threads in a thread pool.

Beamformer. The beamformer generates the multi-pixel, which fills the primary field of view with coherent beams, allowing the tracing of debris through the beam. The beam pointing coefficients are static since no tracking is required and the beam configuration does not change during an observation. The number of beams to generate and their pointing within the primary beam are configurable.

D. Echo Detection

The final stage of the BIRALES space debris pipeline is the data detection module. The aim of this module is to analyze the beamformed data provided by the beamformer module and identify and extract potential space debris candidates. These candidates are persisted into a database to be later retrieved by the orbit determination block. The main stages of the detection module are illustrated in Fig. 6 and described in detail in the following sections.

1. Pre-processing

The beamformed data, which is encoded as complex voltages, is converted into signal-to-noise ratio (SNR) values. An estimate for the background noise value of the system is calculated by taking the average power value of half of the frequency band for a number of samples before the transmitter is initialized. This is then used as the new estimate for the noise.

This input data is subsequently passed through a number of filters. The aim of the filters is to reduce the number of data points that the detection algorithm has to process. In the first filter, the background noise is filtered out by considering data points that are two standard deviations away from the mean as being noise. This effectively removes the bulk of the data given that most of the data being processed is noise.

Secondly, the artefacts introduced by the transmitter are removed by applying a transmission line filter, which applies a threshold on those channels in which a time-independent high SNR is recorded. This ensures that the transmission frequency is not considered by the detection algorithm.

The resultant data could still be noisy. This data is usually characterized by random isolated clusters of data points with a low SNR. In order to remove these data points, and reduce the data set even further, a pepper noise filter is applied. The pepper noise filter removes pixels of data which do not have any neighboring pixels.

2. Clustering Algorithm

The DBSCAN clustering algorithm is used to cluster data points together. It is an unsupervised clustering algorithm that works by grouping points that are closely packed together, expanding clusters in any direction where there are nearby points. This way, it is able to deal with different shapes of clusters. Furthermore, it is robust to noisy data, making it an ideal clustering algorithm to be used for this application. The algorithm is applied to each beam data separately in parallel. The clusters identified by this algorithm are then determined to be potential beam candidates.

3. Validation of the Beam Candidates

The beam candidates are then validated by a number of criteria. The shape of the space debris detection cluster is expected to be linear. Thus, the next stage of the detection module is to identify 'linear clusters'. The algorithm looks for clusters with a high degree of correlation between frequency and time. In order to do so, the RANdom SAmple Consensus (RANSAC) regression algorithm is used.

RANSAC gives a smaller weight to outlier data points, meaning that these data points are ignored. Furthermore, data points that are highlighted as being outliers are removed by the detection algorithm. This means that we not only end up with higher quality clusters (linear clusters with no noise) but it also means that clusters that were eliminated previously because of that data point are no longer deleted. Another optimization that was introduced was to ignore clusters with an unrealistic Doppler shift value.

The remaining validated clusters are then pushed to the space debris queue. The space debris queue is a data

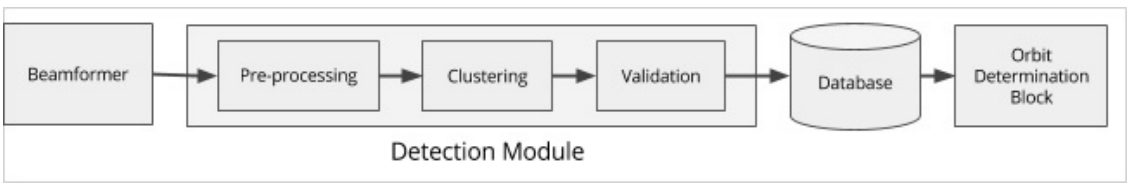

Fig. 6 The main stages of the BIRALES Data Detection Module

structure which was built to hold the validated space debris clusters being identified by the detection algorithm. This data structure ensures that data from the same space debris target is merged into a single space debris object. When the state of the queue changes (by addition or deletion), the space debris candidates are persisted to the database. Candidates that were not modified are not saved again. Once that the candidates are persisted to the database, the user is able to visualize the detections through the monitoring application in real-time. In addition, the system is designed such that the detection data can be used by orbit determination routines.

E. Calibration

Both geometric and inherent instrumental delays will interfere with the true sky visibilities, rendering the visibilities measured by the respective antennas out of phase. This directly results in a reduced SNR as a result of destructive interference occurring in the out of phase fringe patterns obtained from correlating the respective antenna visibilities.

While the geometric delays as a result of the position of the antennas in the field in relation to the position of the measured radio source can be easily derived, the same cannot be said for the inherent instrumental delays which might change as a result of a number of factors. Because of the unpredictability and changing nature of such instrumental delays, a simple but robust instrumental calibration is essential for reducing the resultant lowered sensitivity of an otherwise uncalibrated array. The solution proposed here for the BIRALES receiving array aims to allow calibration to be carried out on a strong point source of relatively stable flux emission in order to characterize instrumental delays. The BIRALES array antennas can only be slewed in altitude, meaning that observation of potential calibration sources can be achieved by slewing to the source's declination and waiting for the target to transit. The observation would thus be carried out at the time where the source RA is equivalent to the local sidereal time. For this reason, the observed incoming visibilities as a source begins transiting the primary beam are expected to change according to the position of the source in the beam itself, as there is no sidereal tracking undergone. Due to both geometric and instrumental effects, the expected clean bell-shaped peak of the transit visibilities of a strong point source are not however achieved, as the incoming visibilities are out of phase as aforementioned. However, it is known that for a given transit of such a source across the field of view, phase differences between the visibilities of the antennas should be zero when the source is exactly in the beam zenith, that is, exactly when the source is halfway through the transit.

1. Stage 1: Peak Source Transit Time Determination

After an observation of a strong source transit, a peak power search is carried out in the correlated visibilities to identify the peak transit of the source through the instrument's beam zenith. The recorded visibilities from all the antennas at each time interval are investigated, in order to determine the time interval at which peak power for the entire transit was measured.

2. Stage 2: Peak Visibilities Calibration

The array visibilities measured at the peak transit time can thus be identified. Subsequently, per-baseline coefficients are obtained for peak visibilities, which give the expected equal gain and phase values for all visibilities at peak transit. The per-antenna coefficients are then obtained by assuming a reference antenna with zero calibration requirements, and obtaining calibration coefficients for all other antennas with respect to it.

Using per-baseline coefficients obtained for baselines subtended by all other antennas with the reference antenna chosen, this allows for the derivation of calibration coefficients for all the antennas with respect to the reference. In order to eliminate possible anomalous antennas interfering with the calibration procedure, any antennas for which coefficients vary beyond a threshold from the rest of the coefficients are left uncalibrated. The calibration coefficients obtained at this stage, however, incorporate corrections for both instrumental and geometric effects, the latter making them only valid for the declination pointing of the calibrator source in question.

3. Stage 3: Geometric Effects Subtraction and Subsequent Addition

The final stage in obtaining the instrumental calibration coefficients involves the separation of geometric effects by subtracting geometric corrections from the calibration coefficients obtained, which are a direct result of the position of the source in the sky. After their removal, the resulting coefficients represent the true corrections required to counter inherent instrumental effects only. These coefficients are then fed back to the real-time processing pipeline, such that the resulting beams are well calibrated.

III. BIRALES Simulator

A simulator of the bistatic radar configuration described above was developed to support analysis and to estimate the system performance. The simulator is designed so that different kind of transmitter and multibeam geometry can be easily defined by the user. A scheme of the architecture of the simulator is reported in Fig. 7. The simulator is made of the following main modules: the passage identification module and the measurements generation module. Given the catalogue of the space objects and the associated TLEs, the passage identification module propagates the motion of the objects using the Simplified General Perturbations 4 (SGP4) model and identifies, in a given time interval, all the passages on the BIRALES sensor. In addition, the module provides the main parameters characterizing the passage, such as the epoch and the required pointings. In case of TLE not available (unknown objects), the definition of the passage epoch and required pointings is done by propagating the state estimates obtained at previous passages (see Sec. V for more details).

Then, for all the passages identified by the passage identification module, the simulator first derives the state of the object at the reference epoch of its TLE. Then, it propagates the motion of the object through its passage on BIRALES using the high-fidelity propagator AIDA (Accurate Integrator for Debris Analysis), which includes the gravitational model EGM2008 up to order 10, the atmospheric drag with the atmosphere model NRLMSISE-00, third body perturbations, and solar radiation pressure with a dual-cone model for Earth shadow. The resulting position and velocity profiles are used to generate the simulated measurements.

The computation of the simulated measurements is described hereafter. A sketch of the geometric configuration of a bistatic radar system is given in Fig. 8. A plane that contains the two relative distance vectors from the transmitter (Tx) and the receiver (Rx), $\boldsymbol{\rho}_{Tx}$ and $\boldsymbol{\rho}_{Rx}$ respectively, and the baseline L can be defined. This plane is usually indicated as bistatic plane and it allows for easy computations of all range relationships. Given the trajectory of the object, the distances ρ_{Tx} and ρ_{Rx} are directly computed using the positions of the two antennas. The time interval Δt between the transmission of the pulse and the reception of the target echo is obtained from

$$\rho_{Tx} + \rho_{Rx} = c\Delta t \tag{1}$$

where c is the speed of light. The bistatic Doppler shift, when ignoring relativistic effects, is computed as

$$\Delta f = \frac{1}{\lambda}(\dot{\rho}_{Tx} + \dot{\rho}_{Rx}) \tag{2}$$

where λ is the wavelength of the transmitted signal and $\dot{\rho}_{Tx}$ and $\dot{\rho}_{Rx}$ are the projections of the Earth-Centered Earth-Fixed (ECEF) target velocity $\boldsymbol{v}$ onto the transmitter-to-target and receiver-to-target line of sight (LOS).
When both Tx and Rx are stationary, the Doppler shift becomes

$$\Delta f = \frac{2v}{\lambda}\cos(\delta)\cos\left(\frac{\beta}{2}\right) \tag{3}$$

Fig. 7 Architecture of BIRALES simulator.

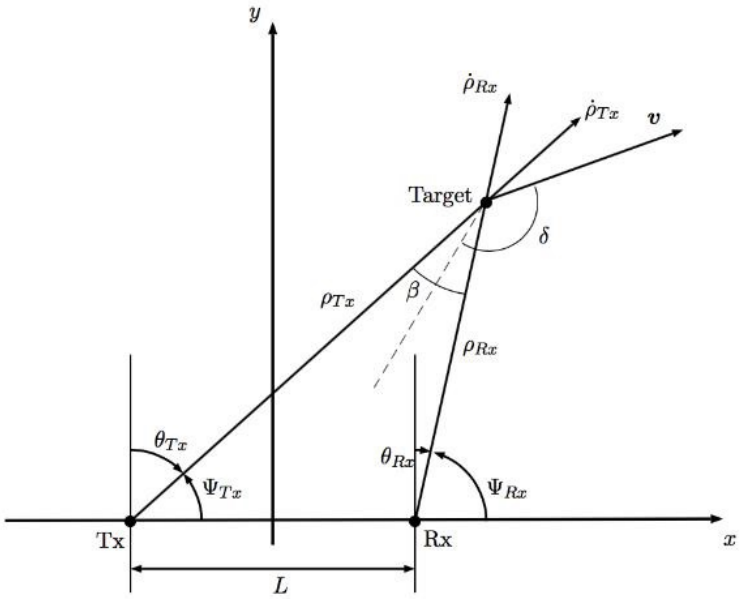

Fig. 8 Geometry of the radar system on the bistatic plane.

Projecting the velocity of the object on the range vectors direction yields

$$\Delta f = \frac{1}{\lambda}(\boldsymbol{v} \cdot \hat{\boldsymbol{\rho}}_{Tx} + \boldsymbol{v} \cdot \hat{\boldsymbol{\rho}}_{Rx}) \tag{4}$$

For each beam of Rx is then possible to compute the received power using the bistatic radar equation

$$P_{Rx} = \frac{P_{Tx} G_{Tx} G_{Rx} \lambda^2 \sigma_b}{4\pi^3 \rho_{Tx}^2 \rho_{Rx}^2} \tag{5}$$

where P_{Tx} is the transmitter power, G_{Tx} and G_{Rx} are the antenna gains, and σ_b is the radar cross section. Where needed, the information on the satellite radar cross section are taken from a Space-Track catalogue downloaded on October 10, 2014. At each time step the ranges ρ_{Tx} and ρ_{Rx} are obtained from orbit propagation and the antenna gains are updated using an elliptical model for the beam:

$$G_{dB} = G_{dB0} - 12\left(\left(\frac{\Delta\gamma_1}{BW_{\gamma_1}}\right)^2 + \left(\frac{\Delta\gamma_2}{BW_{\gamma_2}}\right)^2\right) \tag{6}$$

where $G_{dB} = 10\log_{10} G$, G_{dB0} is the reference gain of the antenna in decibel, $\Delta\gamma_1$ and $\Delta\gamma_2$ are the angular deviations from beam center, and the beamwidths on the two axes of the ellipse are BW_{γ_1} and BW_{γ_2}. Once the received power is obtained, the SNR value is computed as

$$\text{SNR} = 10\log_{10}\frac{P_{Rx}}{k_B B_n T_0} \tag{7}$$

in which k_B is the Boltzmann constant, B_n is the bandwidth of the receiver and T_0 is the noise temperature at the receiver. Figure 9 reports the illustration of a passage through the 32 beams distributed in the field of view of the sensor. The beams and the angles profiles are plotted in the $\Delta\gamma_1 - \Delta\gamma_2$ plane and coloured according to their maximum value of SNR, normalized with respect to the maximum SNR among all beams. Non-illuminated beams are colored in black.

The resulting simulated measures are organized in a text file, reporting the measured Δt, Δf, and SNR for each beam and for each time. The text file is the input to the OD algorithm.

IV. Orbit Determination Algorithm: First Passage Analysis

This section illustrates the orbit determination algorithm for the case of the first passage of the tracked object inside the FoV of the sensor. The cases of known and unknown object are studied, and the differences in the implementations

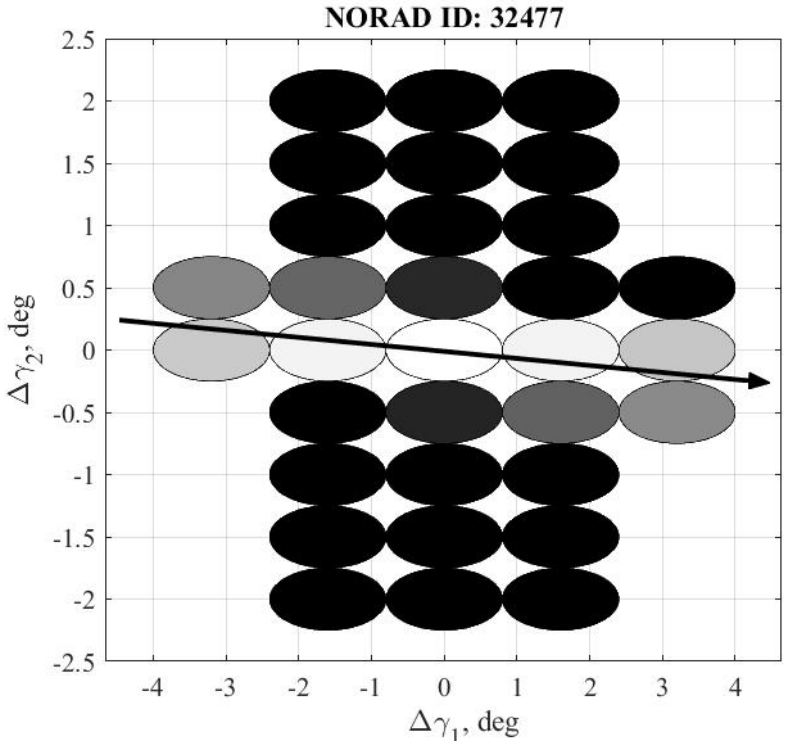

Fig. 9 Passage inside the receiver FoV for object NORAD ID 32477.

are highlighted. The description of the algorithm follows the scheme presented in [1].

A. Known Objects

The case of known object refers to the OD process performed for an object whose TLE is available to the user. In this situation, the orbit determination process is divided in two phases. The first phase consists in evaluating the angular deviations $\Delta\gamma_1$ and $\Delta\gamma_2$ of the Resident Space Object (RSO) starting from the knowledge of SNR measurements. Then, the object position and velocity vectors are estimated using a least square fit.

The evaluation of $\Delta\gamma_1$ and $\Delta\gamma_2$ is performed by assuming that the track of the object inside the FoV of the sensor can be approximated by a straight or slightly curved line. Thus, the time history of the two variables can be expressed as:

$$\begin{cases} \Delta\gamma_1 = a_1 t + a_0 \\ \Delta\gamma_2 = b_1 t + b_0 \end{cases} \tag{8}$$

for the linear model, and

$$\begin{cases} \Delta\gamma_1 = a_2 t^2 + a_1 t + a_0 \\ \Delta\gamma_2 = b_2 t^2 + b_1 t + b_0 \end{cases} \tag{9}$$

for the quadratic model, where t is the time elapsed from the first measurement obtained during the passage of the object inside the FoV of the sensor. The estimation of the coefficients a_0, a_1, b_0 and b_1 for the first model and a_0, a_1, a_2, b_0, b_1 and b_2 for the second model is divided in two steps (referred to as S1 and S2 in the followings). In S1, the knowledge of the level of the measured SNR for each beam and the TLE of the observed object are combined. A representation of the results of the two steps for the case of quadratic model is shown in Fig. 10. The procedure goes through the following steps:

S1-1. For each illuminated beam, identify the time instant of maximum illumination, the related SNR, and the angular pointing of the center of the beam.

S1-2. Perform a curve fit that minimizes the angular displacement from each beam centre at the time of the maximum received power. The selected weights are the normalized values of the SNR, using as a reference the maximum SNR among all beams (see Fig. 10a).

S1-3. Evaluate the $\Delta\gamma_1$ and $\Delta\gamma_2$ time histories starting from the knowledge of the TLE of the observed object at a specific time epoch before the observation epoch and propagating the initial state vector by means of SGP4. This fictitious observation process provides the trace the object would have inside the receiver FoV if the dynamic was described by the approximated SGP4 model (see Fig. 10b).

S1-4. Rotate the solution obtained with step S1-2 along the direction provided by step S1-3 (see Fig. 10c).

The solution obtained with step S1 provides a rough estimate of the angular deviation profile inside the receiver FoV. In S2, the solution is refined with a least square aimed at minimizing the residuals between the measured SNRs and their estimates, obtained with the $\Delta\gamma_1(t)$ and $\Delta\gamma_2(t)$ guesses. At convergence, the procedure provides the time history of the angular deviations inside the receiver FoV according to the selected model (see Fig. 10d). This is repeated for both fitting models. Then, the linear or quadratic model is selected, according to the magnitude of the computed residuals at the end of the least squares procedure (step S2).

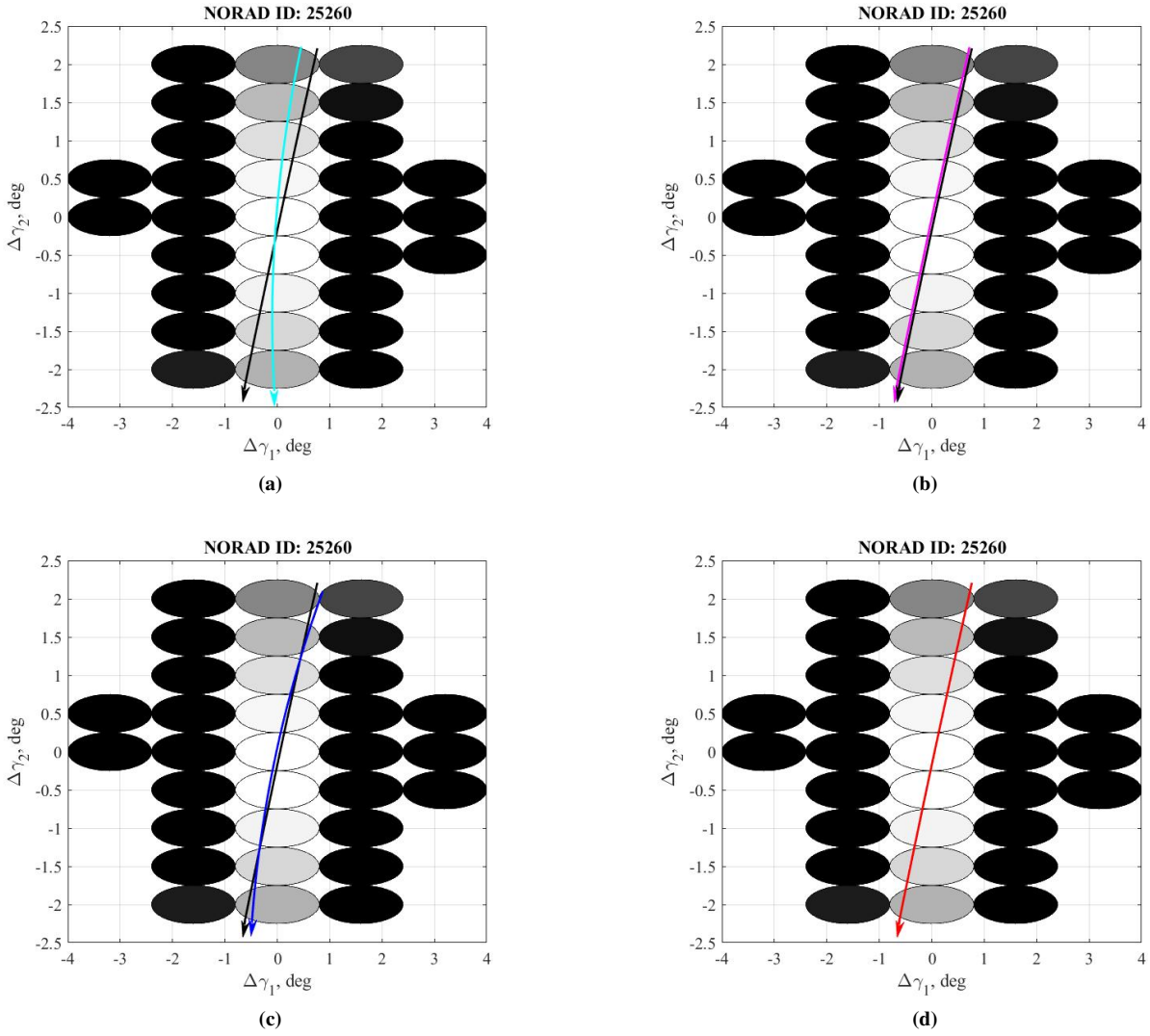

Fig. 10 Angular deviation time history identification inside the receiver FoV for object NORAD ID 25260 (quadratic model): (a), first guess generation (cyan line, step S1-2), (b) TLE propagation (magenta line, step S1-3), (c) first guess refinement (blue line, step S1-4), (d) estimated $\Delta\gamma_1(t)$-$\Delta\gamma_2(t)$ profile (red line, step S2)

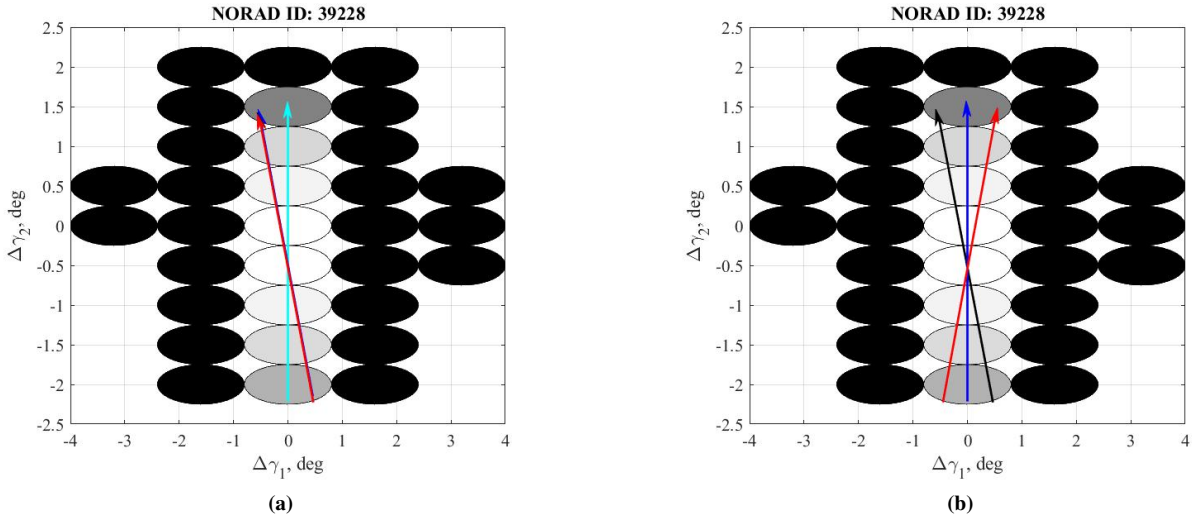

Fig. 11 $\Delta\gamma_1(t) - \Delta\gamma_2(t)$ definition for object NORAD ID 39228 in case of available ((a), known object) and not available ((b) TLE, unknown object)

Once the angular deviations profiles of the RSO are obtained, the OD process starts. The aim of the OD process is to estimate the state of the object at the epoch of the first measurement obtained during its passage in the FoV of the sensor. The process consists of a nonlinear least square optimization to match the orbital trajectory with the range measurements, the Doppler shift measurements and the angular deviations time histories previously computed. The algorithm starts from an initial guess and propagates it in time using the high-fidelity propagator AIDA. The algorithm is the following:

OD 1. Consider an initial guess for the RSO state vector at the epoch of the first measurement. In the case of known object, the guess is obtained by propagating the state vector provided by the TLE of the object till the first observation epoch by means of SGP4.

OD 2. Propagate the initial state and compute, for each observation instant, the state vector of the observed object, deriving the values of slant range, Doppler shift and the angular deviations.

OD 3. Evaluate the residuals of the four quantities with respect to the measured values.

OD 4. Update the initial guess.

The algorithm provides the estimated state vector at the epoch of the first observation and the related covariance matrix.

B. Unknown Objects

The case of unknown object refers to OD process performed for an object whose TLE is not available to the user. The algorithm described in the previous section is slightly modified in this case. The unavailability of the TLE does not allow to exploit the knowledge of the state vector for both the estimation of the angular deviations profiles of the object, and the generation of the first guess for the orbit determination process.

The first issue is solved by reducing the S1 procedure to its first two steps (S1-1 and S1-2): the first guess for $\Delta\gamma_1(t)$ and $\Delta\gamma_2(t)$ is generated considering only the available SNR measurements. Moreover, during the S2 procedure, the radar cross section of the object is included in the set of unknowns of the least square fit.

Unfortunately, the simplification of the S1 procedure for the first guess generation yields to symmetry problems in the definition of the angular deviations profiles. Symmetry problems arise when, during the passage of an object inside the receiver FoV, only a single column of beams is illuminated. In this case, the initial guess for the $\Delta\gamma_1(t)$-$\Delta\gamma_2(t)$ profile is a vertical line connecting the center points of the illuminated beams that represents the symmetry axis between the real profile and the symmetric one, characterised by the same SNR measurements. An example is shown in Fig. 11b. As the initial guess is equidistant from the two possible profiles, the solution may converge to both the exact and the specular solution. Figure 11 shows the results of the definition of the angular profiles for object NORAD ID 39228 in case of available (Fig. 11a) and unavailable (Fig. 11b) TLE. In the first case, the identification of the theoretical track provided by the TLE (step S1-3) allows to rotate the initial guess towards the right solution, thus skipping any symmetry

condition. In the case of unknown object, instead, the first guess is exactly half way between the real track and the symmetric one, and step S2 converges to the wrong solution. This leads to a completely wrong orbit determination process. At present, the occurrence of symmetry during the passage of an unknown object represents a weak point of the algorithm.

The first guess (GG) for the orbit determination process is generated assuming a motion on a circular orbit. The algorithm is the following:

GG 1. Sort the beams of the receiver according to their maximum measured SNR during the observation window.

GG 2. Identify the beam with maximum illumination during the passage of the object and the corresponding observation epoch t_1.

GG 3. Assume that the object passes at the centre of the beam at t_1, consider the line of sight of that beam and identify on it the point of minimum distance between this direction and the line of sight of the transmitter at epoch t_1. Define the computed vector as $\boldsymbol{r}_1$. Under the considered assumptions, $\boldsymbol{r}_1$ represents the position vector of the observed object at epoch t_1.

GG 4. Assume a circular motion for the object, consider the second beam of the list and obtain the position vector $\boldsymbol{r}_2$ at epoch t_2 as the intersection between the line of sight of the beam and a position vector of the previously computed magnitude.

GG 5. Evaluate the orbital parameters starting from $\boldsymbol{r}_1$ and $\boldsymbol{r}_2$.

GG 6. Compute the position and velocity vectors of the RSO at the first observation epoch.

The accuracy in the determination of the first guess is strictly related to the validity of the approximations made in the process. In particular, the accuracy of the two position vectors $\boldsymbol{r}_1$ and $\boldsymbol{r}_2$ drastically decreases as the actual position of the object at t_1 and t_2 moves away from the centre of the selected beams, and this is likely to occur when the maximum detected SNR of those beams is low. This is the reason why the two beams with the largest measured SNRs are selected. The same approach is used for highly-elliptical orbits although the assumption of circular orbit loses its validity.

Once the first guess is defined, the OD process is performed including only gravitational effects in the object dynamics due to the unavailability of the ballistic coefficient of the object.

C. Numerical Simulations

The results of the performed numerical simulations are presented in this section. An observation window of two days is assumed, covering the range May 25-26, 2016. The main characteristics of the transmitter and the receiver in the analysed configuration are presented in Table 1.

Table 1 Transmitter and receiver characteristics.

	Latitude	Longitude	Altitude	Diameter	Power
TX	39°45′31″N	9°27′01″E	205 m	7 m	10 kW
RX	44°31′25″N	11°38′59″E	25 m	-	-

The beam configuration of the receiver is the one shown in Fig. 9, with 32 beams in symmetric configuration. The analysis covers both the cases of known and unknown objects, studying the impact of measurement noise on the accuracy of the orbit determination results.

1. Known Objects

The case of known object with no noise measurements represents the first test for the tool. Measurement noise represents the deviation between the reality and the mathematical model used to describe it. The number of catalogued objects is 5100, and only 283 can be observed (i.e., have a passage in the FoV of the sensor and generate a detectable SNR level). The reference condition for the error computation is evaluated by propagating the state vector provided by the TLE using AIDA up to the epoch of the first measurement. Table 2 shows the results of the accuracy in position in terms of 50$^{\text{th}}$ and 75$^{\text{th}}$ percentile of the position error in radial direction ($\varepsilon_{p,rad}^{50\%}$ and $\varepsilon_{p,rad}^{75\%}$), 50$^{\text{th}}$ percentile of the position error ($\varepsilon_{p}^{50\%}$) and of the standard deviation in position ($\sigma_{p}^{50\%}$). As can be seen, all errors in positions are below 1 m. Moreover, the analysis shows that all objects have a position error in radial direction lower than 100 m. This trend is quite expected, as the investigated case is the simplest possible, i.e. no disturbances introduced by measurement noise.

Table 2 Accuracy in position for the case of known object with no measurement noise.

$\varepsilon_{p,rad}^{50\%}$	$\varepsilon_{p,rad}^{75\%}$	$\varepsilon_{p}^{50\%}$	$\sigma_{p}^{50\%}$
0.176 m	0.506 m	0.91 m	0.56 m

The performances of the simulator in terms of accuracy in velocity for all the objects with radial error in position lower than 100 m are shown in Table 3. The selected performance indeces are:

1) 50$^{\text{th}}$ percentile of the error in transversal velocity ($\varepsilon_{v,tr}|^{50\%}_{\varepsilon_{p,rad}<100\,\text{m}}$)
2) 75$^{\text{th}}$ percentile of the error in transversal velocity ($\varepsilon_{v,tr}|^{75\%}_{\varepsilon_{p,rad}<100\,\text{m}}$)
3) 50$^{\text{th}}$ percentile of the standard deviation in velocity ($\sigma_{v}|^{50\%}_{\varepsilon_{p,rad}<100\,\text{m}}$).

As expected, all terms are very low, and far below 1 m/s.

Table 3 Accuracy in velocity for the case of known objects with no measurement noise.

$\varepsilon_{v,tr}\|^{50\%}_{\varepsilon_{p,rad}<100\,\text{m}}$	$\varepsilon_{v,tr}\|^{75\%}_{\varepsilon_{p,rad}<100\,\text{m}}$	$\sigma_{v}\|^{50\%}_{\varepsilon_{p,rad}<100\,\text{m}}$
0.015 m/s	0.042 m/s	0.04 m/s

It is now interesting to study the performance of the tool in case of presence of measurement noise. The first analysis is performed by assuming a noise on the slant range (SR) and Doppler shift (DS) measurements. The noise in the slant range is modelled with a Gaussian distribution with zero mean and standard deviation of 3 m. The Doppler shift noise is modelled by assuming a resolution of 20 Hz.

The results for the case under study are shown in Table 4, second row. As can be seen, the accuracy is worse than in the previous case, though still all objects show a radial error in position lower than 100 m. In particular, position errors increase of one order of magnitude, whereas the decrease in accuracy for the velocity components is more significant. Overall, the influence of the introduced measurement noise is evident, though acceptable.

The measurement noise is finally added to the SNR profiles as a white Gaussian noise, assuming a ratio of 30 dB between the nominal signal and the added white noise. The results of a simulation including all the three contributions to the measurement noise are shown in the third row of Table 4. As can be seen, the combination of all three measurement noises causes a relevant decrease in the accuracy of the results in both position and velocity with respect to the ideal case with no noise, whereas the difference with respect to the case of measurement noise in only SR and DS is less evident.

2. Unkown Objects

The performance of the sensor in case of unknown objects is now investigated. The inaccuracy in the pointing of the receiver due to the unavailability of the TLE of the object is here modelled as a random error of ±2.5 deg in the elevation of the receiver with respect to the pointing computed by the simulator.

The results of unknown object and no measurement noise are shown in Table 5, first row. A comparison with the analogous case of known object shows how the error significantly increases when the object is not known a priori. This can be explained with the fact that the unavailability of the TLE in some cases prevents the algorithm from precisely identifying the angular deviation profiles of the object, leading to a partially or totally wrong orbit determination. However, the algorithm is still able to perform the orbit determination granting a radial error in position below 100 m for more than the 80 per cent of the cases.

If measurement noise is considered, the results shown in the second and third rows are obtained. While the introduction of measurement noise on slant range and Doppler shift has a stronger effect on the accuracy in velocity, the combination of all three contributions drastically increases all the errors. The comparison between the two extreme cases of the presented simulations (known objects without measurement noise and unknown objects with all measurement noises) clearly shows how the performance of the algorithm strongly depends on the availability of the TLE of the object and the noise level. Overall, the last case represents, as expected, the most critical situation.

Figure 12 shows the trend of the cumulative error in transversal velocity for all the objects with $\varepsilon_{p,rad}$ lower than 100 m. It is interesting to study the trend of the cumulative error in the most critical case (red line). As can be seen, while more than 90 per cent of the objects show an error in transversal velocity lower than 10 m/s, few objects have much larger errors, essentially due to symmetry problems.

Table 4 Performance of the sensor for the case of known object, standard beam configuration.

	n_{obj}	$\varepsilon_{p,rad}^{50\%}$	$\varepsilon_{p,rad}^{75\%}$	$\varepsilon_{p}^{50\%}$	$\sigma_{p}^{50\%}$	$\varepsilon_{v,tr}\vert_{\varepsilon_{p,rad}<100\,\mathrm{m}}^{50\%}$	$\varepsilon_{v,tr}\vert_{\varepsilon_{p,rad}<100\,\mathrm{m}}^{75\%}$	$\sigma_{v}\vert_{\varepsilon_{p,rad}<100\,\mathrm{m}}^{50\%}$
No noise	283	0.176 m	0.506 m	0.91 m	0.56 m	0.015 m/s	0.042 m/s	0.04 m/s
Noise in SR and DS	278	1.62 m	3.48 m	6.96 m	101.6 m	1.4 m/s	3.05 m/s	6.6 m/s
Noise in SR, DS and SNR	281	4.13 m	7.96 m	24.5 m	102.5 m	1.4 m/s	3.33 m/s	6.65 m/s

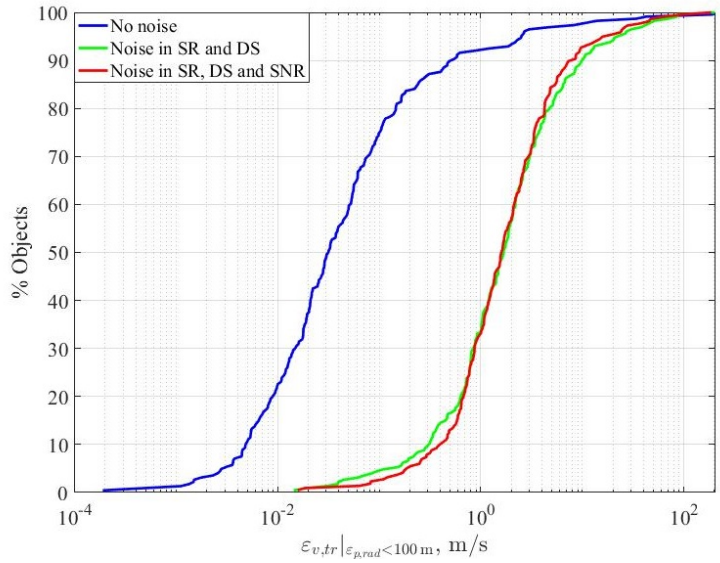

Fig. 12 Cumulative error in transversal velocity for all objects with $\varepsilon_{p,rad}$ lower than 100 m (unknown object, standard configuration).

3. Alternative Beam Configurations

The analysis presented in the previous section has shown how the case of unknown object represents the most critical one, with a significant decrease in accuracy in case of measurement noise. As the configuration of the pattern of beams of the receiver represents the main available degree of freedom, it is now interesting to study the performances of the sensor with different beam configurations. In this section, two alternative beam configurations are presented, and the analysis is done for the case of unknown objects with noise in all measurements.

The first beam configuration is presented in Fig. 13 (right): the centers of the 32 beams are slightly shifted to obtain beam overlapping. The second beam configuration is shown on the left in the same figure: the number of beams is doubled with respect to the nominal configuration, so that the overall field of view of the sensor is increased. A comparison of the performance of the sensor in the standard configuration with these two alternative configurations is presented in Table 6. As can be seen, both configurations allow to increase the accuracy of the orbit determination process in position and velocity. In particular, while the overlapped beams configuration shows better performance in terms of position error, a higher accuracy in velocity can be obtained with the increased FoV configuration.

Table 5 Performance of the sensor for the case of unknown object, standard beam configuration.

	n_{obj}	$\varepsilon_{p,rad}^{50\%}$	$\varepsilon_{p,rad}^{75\%}$	$\varepsilon_{p}^{50\%}$	$\sigma_{p}^{50\%}$	$\varepsilon_{v,tr}\vert_{\varepsilon_{p,rad}<100\,\mathrm{m}}^{50\%}$	$\varepsilon_{v,tr}\vert_{\varepsilon_{p,rad}<100\,\mathrm{m}}^{75\%}$	$\sigma_{v}\vert_{\varepsilon_{p,rad}<100\,\mathrm{m}}^{50\%}$
No noise	276	0.64 m	8.9 m	4.18 m	1.2 m	0.032 m/s	0.1 m/s	0.061 m/s
Noise in SR and DS	277	2.66 m	16.2 m	13.3 m	111 m	1.68 m/s	3.76 m/s	6.7 m/s
Noise in SR, DS and SNR	273	8.26 m	46.7 m	49.9 m	111.4 m	1.6 m/s	3.365 m/s	6.7 m/s

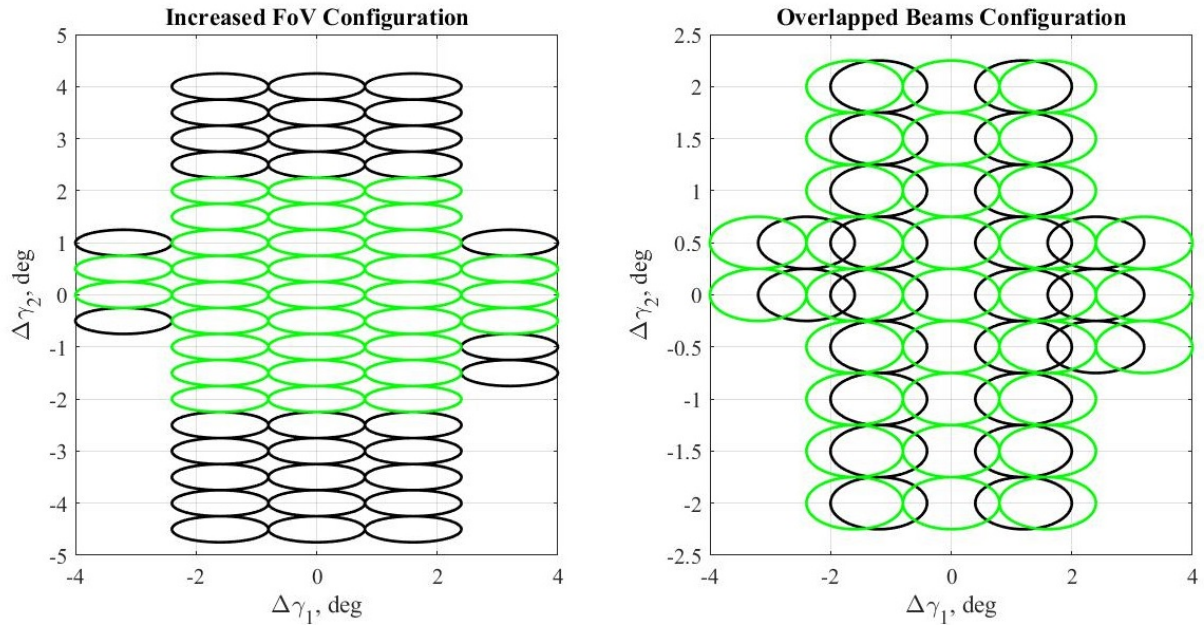

Fig. 13 In black: increased FoV configuration (left) and overlapped beam configuration (right). In green: standard beam configuration.

Table 6 Comparison of the performance of the algorithm with different beam configurations of the receiver (case of unknown objects, measurement noise in SR, DS and SNR).

	n_{obj}	$\varepsilon_{p,rad}^{50\%}$	$\varepsilon_{p,rad}^{75\%}$	$\varepsilon_{p}^{50\%}$	$\sigma_{p}^{50\%}$	$\varepsilon_{v,tr}\vert_{\varepsilon_{p,rad}<100\,\mathrm{m}}^{50\%}$	$\varepsilon_{v,tr}\vert_{\varepsilon_{p,rad}<100\,\mathrm{m}}^{75\%}$	$\sigma_{v}\vert_{\varepsilon_{p,rad}<100\,\mathrm{m}}^{50\%}$
Standard Configuration	273	8.26 m	46.7 m	49.9 m	111.4 m	1.6 m/s	3.365 m/s	6.7 m/s
Overlapped beams	214	5.09 m	12.6 m	27.9 m	107.5 m	1.59 m/s	3.33 m/s	6.86 m/s
Increased FoV	426	5.63 m	14.21 m	28.26 m	81.01 m	0.7 m/s	1.65 m/s	3.24 m/s

Figure 14 shows the same plot of Fig. 12 for the three analysed configurations: again, it is evident how both alternative configurations guarantee a general improvement of the accuracy in velocity.

V. Orbit Determination Algorithm: Repeated Passages

The analysis presented in Sec. IV was performed by considering the first passage, i.e. assuming to have no information about the object from previous passages. In this section, the case of repeated passages of the same object on the Medicina receiver ground station will be considered. The analysis will be dedicated to the second passage for both cases of known and unknown objects. In both cases, the results obtained with the batch OD algorithm described in Sec. IV and applied to the second passage are compared with the results of a sequential OD algorithm in which the a priori estimate is provided by the results of the batch OD algorithm applied to the first passage. The same transmitter and receiver characteristics shown in Table 1 and the standard beam configuration are considered, assuming an observation window of one week starting from October 2, 2017.

A. Known Objects

The starting point of the analysis for the case of known objects is represented by the TLE reference epoch of each object in the catalogue. The passage scheduler described in Sec. III allows to identify the epoch of the first passage on the selected receiver. For all observed objects, an estimated state vector $\hat{\boldsymbol{x}}_{1st}$ and related covariance matrix $\boldsymbol{C}_{\hat{\boldsymbol{x}}\hat{\boldsymbol{x}}_{1st}}$ is obtained with the algorithm described in Sec. IV. These estimates are then propagated in time to the epoch of the

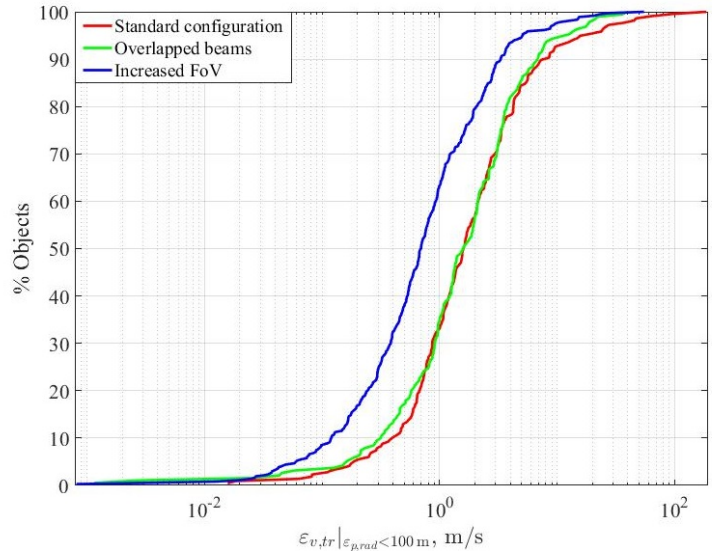

Fig. 14 Cumulative error in transversal velocity for objects with $\varepsilon_{p,rad}$ lower than 100 m (unknown object, noise in SR, DS, SNR).

Table 7 OD estimates accuracy for the second passage (known object)

	EKF	UKF	EKF$_{TLE}$	UKF$_{TLE}$	Batch
$< \varepsilon_p >$	217 km	25 km	106.9 m	48.8 m	76.7 m
$< \sigma_p >$	6.4 m	8.8 m	10.2 m	9.1 m	126 m
$< \varepsilon_v >$	6.2 km/s	1.2 km/s	5.3 m/s	1.5 m/s	20.5 m/s
$< \sigma_v >$	0.3 m/s	0.5 m/s	0.4 m/s	0.5 m/s	12.3 m/s

second passage, providing an a priori knowledge of the state of the object $\bar{\boldsymbol{x}}_{2nd}$ and related covariance $\boldsymbol{C}_{\bar{\boldsymbol{x}}\bar{\boldsymbol{x}}_{2nd}}$ at the first time instant of the second observation window. Finally, this estimate is refined by using a sequential filter on the basis of the available measurements.

The results of the numerical simulations are presented hereafter. Figure 15 shows the distribution of the position error for all objects that were observed in both passages. Only 99 objects could be observed in both passages out of the 330 observed during the first one. The blue dots represent the accuracy of the estimates at the epoch of the first passage, whereas the red dots represent the accuracy of the a priori estimates, i.e. the accuracy of the estimates obtained at the epoch of the first passage when propagated to the epoch of the second passage. As can be seen, the average error increases of at least three orders of magnitude while propagating the estimates from the first to the second passage epoch.

The implementation of the sequential filter for the computation of the state of the objects at the epoch of the second passage was based on two different approaches. A first approach, in which the reference orbit for the sequential filter is provided by the available a priori estimate, and a second approach in which the reference orbit is generated by propagating the available TLE of the object.

Table 7 shows the results of the analysis. The results are expressed in terms of mean error in position $< \varepsilon_p >$, mean standard deviation in position $< \sigma_p >$, mean error in velocity $< \varepsilon_v >$ and mean standard deviation in velocity $< \sigma_v >$ for the estimates at the epoch of the second passage. Two different sequential filters for both cases were tested: an Extended Kalman Filter (EKF) and an Unscented Kalman Filter (UKF), and results were compared with the results of the batch algorithm (see Sec. IV), i.e. what could be obtained with no a priori knowledge about the state of the objects (last column). The second and third columns show the results obtained without the knowledge of the TLE of the objects. As can be seen, the UKF allows to obtain higher accuracy with respect to the EKF. However, both approaches turn out to be less accurate than the batch algorithm. That is, if only the a priori estimate of the objects is exploited, no advantages can be obtained with respect to the standard approach described in Sec. IV. This can be explained considering the

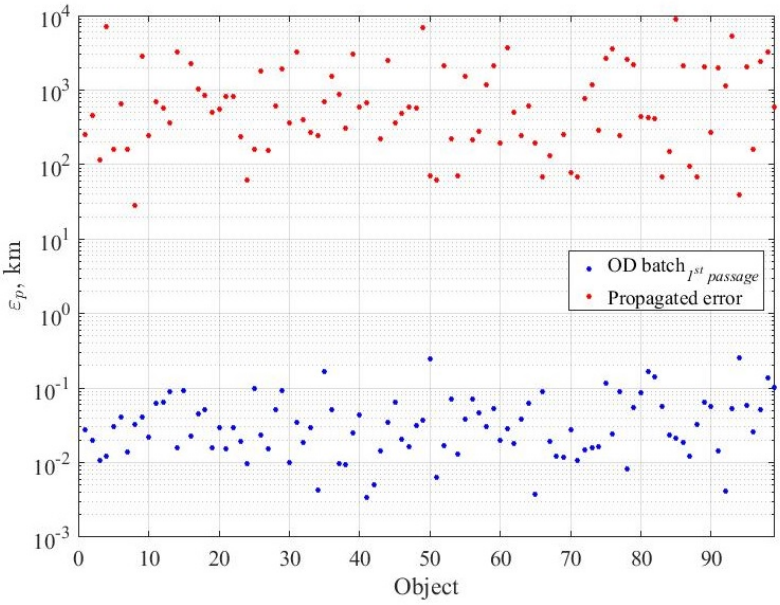

Fig. 15 Error distribution for the estimates at the epoch of the first passage (blue) and for the a priori estimates at the second passage (red).

large error of the a priori estimates. The fourth and fifth columns, instead, show the average accuracy obtained by using Extended and Unscented Kalman filters in which the reference orbit is obtained by propagating the available TLE (EKF$_{TLE}$ and UKF$_{TLE}$ respectively). As can be seen, the average accuracy is significantly higher than what obtained without the use of the TLE, and the UKF$_{TLE}$ represents, overall, the best solution among all the considered ones.

B. Unknown Objects

In the case of unknown objects, the epoch of the second passage is not known a priori. The starting point of the analysis is represented by the estimate of the state of the object at the epoch of the first passage $\hat{\boldsymbol{x}}_{1st}$. This estimate is then propagated in the passage scheduler and an estimate of the epoch of the second passage is obtained, along with the estimated required pointing directions for the transmitter and receiver. The accuracy of this estimate is strictly related to the accuracy of the propagated state estimate: if the error is too large, the second passage may be shifted in time and the object completely lost. For those objects whose predicted second passage is sufficiently accurate, the available a priori estimate of the state of the object is then refined by means of a sequential filter on the basis of the available measurements, and the procedure is repeated. Therefore, for the case of unknown objects, the analysis focuses on two aspects: the number of re-observed objects and the accuracy of the obtained estimates.

Figure 16a shows the distribution of the position error for all the objects observed during the first passage. The blue dots represent the accuracy of the estimates at the epoch of the first passage, whereas the red dots represent the accuracy of the propagated estimates at the epoch of the predicted second passage. As can be seen, in most of the cases the propagated error is very large, affecting the recovery of the object in the second passage. Figure 16b shows in bold the objects that are actually re-observed during the second passage. As expected, they show the lowest propagated errors among all objects. It is evident, however, that these objects represent a low percentage with respect to the number of objects observed at the first passage: approximately 90% of the objects is lost. This is related to the large propagated error, that in turn is due to the large time intervals that in average are needed between one observation window and the next one. This suggests the possibility of coupling the receiver with other ground station receivers, with the aim of increasing the number of re-observations, thus allowing to reduce the number of lost objects. This last aspect represents a future development of the research.

For all the observed objects, an analysis of the performance of different sequential filters was carried out. In this case, given the unavailability of the TLE of the objects, the reference orbit for the filters was obtained only by propagating the available estimates from the first passage. Table 8 shows a comparison between EKF, UKF and the standard batch

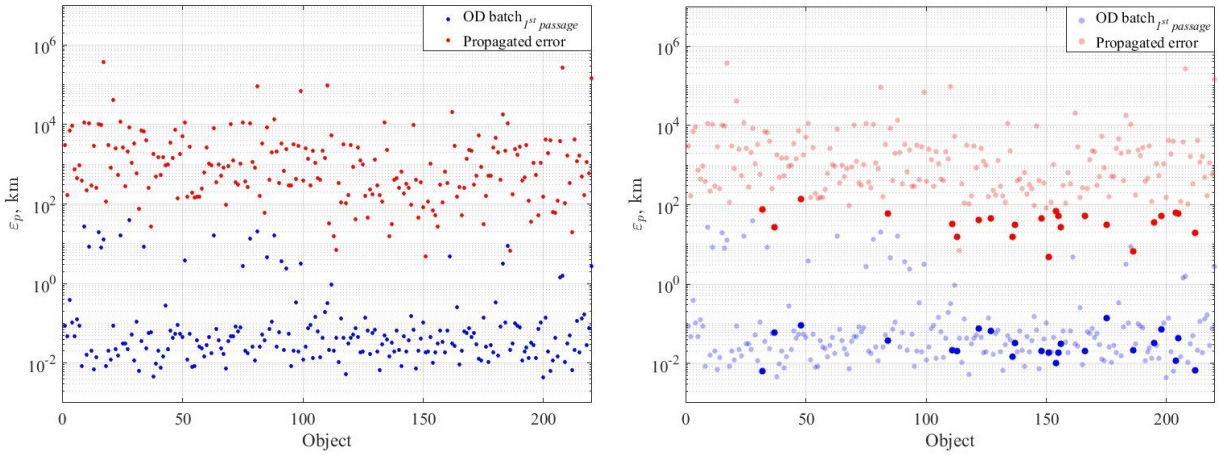

Fig. 16 Error distribution for the estimates at the epoch of the first passage (blue) and for the propagated estimates at the epoch of the theoretical second passage (red).

Table 8 OD estimates accuracy for the second passage (unknown object)

	EKF	UKF	Batch
$\varepsilon_p^{50\%}$	625.9 m	29.4 m	41.5 m
$\sigma_p^{50\%}$	8.2 m	8.6 m	107.9 m
$\varepsilon_v^{50\%}$	15.8 m/s	0.6 m/s	8.4 m/s
$\sigma_v^{50\%}$	0.3 m/s	0.4 m/s	8.0 m/s

algorithm. As can be seen, UKF allows to obtain the best performance.

VI. Conclusion

The performance of the BIRALES radar sensor in terms of the achievable accuracy of the orbital estimation process on a catalogue of resident space objects has been assessed through numerical simulations. A simulator was developed to produce observation data in terms of SNR, Doppler shift, and time delay profiles during the passage in the volume defined by the intersection of the transmitter and receiver beams. The simulator allowed to test different beamforming geometries for the receiver, using different locations for each beam. The simulations show that the sensor, provided with its tailored OD algorithm, can estimate the orbital states with reasonable accuracy with just a single pass for most objects in the catalogue. The analysis was then extended to the case of the second passage, showing the performance of the sensor in both cases of known and unknown objects. This preliminary analysis and results will be extended in future works. The simulated beams will be adapted to their final optimized configuration, the ranging will be modelled based on the performance of the final transmitter, and the simulator and the OD algorithm will be calibrated using data from real observation campaigns. In addition, different beamforming geometry will be tested to support the possible upgrade strategies for the Northern Cross, taking into account the complete refurbishment of the antenna. The analysis on repeated passages will be extended by considering the sinergy with other receiver sensors, with the aim of increasing the number of tracked objects.

Acknowledgments

The authors acknowledge the support of the Italian Space Agency and the Italian National Institute of Astrophysics through the grant agreement n. 2015-028-R.O. (Space Debris – IADC activities support and SST pre-operative validation). The Radio Frequency Transmitter is located at the Italian Joint Test Range of Salto di Quirra in Sardinia.

The Northern Cross radiotelescope is a facility of the University of Bologna operated under agreement by the Radio Astronomy Institute of the Italian National Institute of Astrophysics.

References

[1] Di Lizia, P., Massari, M., Losacco, M., Bianchi, G., Mattana, A., Pupillo, G., Bortolotti, C., Roma, M., Morselli, A., Armellin, R., Magro, A., Cutajar, D., Reali, M., and Portelli, C., "Performance assessment of the multibeam radar sensor BIRALES for space surveillance and tracking," *7th European Conference on Space Debris*, Vol. 7, edited by T. Flohrer and F. Schmitz, ESA Space Debris Office, 2017.

[2] Flohrer, T., Krag, H., Lemmens, S., Bastida Virgili, B., Merz, K., and Klinkrad, H., "A Statistical Look at ESA's Conjunction Event Predictions," *6th European Conference on Space Debris*, ESA Special Publication, Vol. 723, edited by L. Ouwehand, 2013, p. 51. Provided by the SAO/NASA Astrophysics Data System.

[3] Pardini, C., and Anselmo, L., "Re-entry predictions of three massive uncontrolled spacecraft," *23rd International Symposium on Space Flight Dynamics*, 2012.

[4] European Parliament, and Council, "Decision No 541/2014/EU of the European Parliament and of the Council of 16 April 2014 establishing a Framework for Space Surveillance and Tracking Support," , Apr. 2014. URL `http://data.europa.eu/eli/dec/2014/541(1)/oj`.

[5] ESA, "ESA's space situational awareness," , Mar. 2017. URL `http://www.esa.int/Our_Activities/Operations/Space_Situational_Awareness/About_SSA`.

[6] Morselli, A., Di Lizia, P., Bianchi, G., Bortolotti, C., Montebugnoli, S., Naldi, G., Perini, F., Pupillo, G., Roma, M., Schiaffino, M., Mattana, A., Salerno, E., Magro, A., Adami, K. Z., Armellin, R., Lazzareschi Sergiusti, A., Villadei, W., Dolce, F., Reali, M., and Paoli, J., "A new high sensitivity radar sensor for space debris detection and accurate orbit determination," *Metrology for Aerospace (MetroAeroSpace)*, 2015.

[7] Montebugnoli, S., Bianchi, G., Monari, J., Naldi, G., Perini, F., and Schiaffino, M., "BEST: Basic Element for SKA Training." *Wide Field Astronomy Technology for the Square Kilometre Array*, 2009, p. 58.

[8] Bianchi, G., Bortolotti, C., Cattani, A., Fiocchi, F., Maccaferri, A., Mattana, A., Morsiani, M., Naldi, G., Perini, F., Porfido, A., Pupillo, G., Roma, M., Rusticelli, S., Schiaffino, M., Urru, E., Di Lizia, P., Losacco, M., Massari, M., Borg, J., Cutajar, D., Magro, A., Reali, M., and Villadei, W., "A new approach to LEO space debris survey: the Italian multibeam bi-static radar 'BIRALES'," *1st IAA Conference on Space Situational Awareness (ICSSA)*, 2017.